# *Hydrogenation of Tetralin Over Ir Catalysts Supported on Titania-Modified SBA-16*

**Brenda C. Ledesma, Verónica A. Vallés, Lorena P. Rivoira, María L. Martínez, Oscar A. Anunziata & Andrea R. Beltramone**

**Catalysis Letters**

ISSN 1011-372X
Volume 144
Number 5

Catal Lett (2014) 144:783-795
DOI 10.1007/s10562-014-1222-8


Springer

Catal Lett (2014) 144:783–795
DOI 10.1007/s10562-014-1222-8

# Hydrogenation of Tetralin Over Ir Catalysts Supported on Titania-Modified SBA-16

**Brenda C. Ledesma · Verónica A. Vallés · Lorena P. Rivoira · María L. Martínez · Oscar A. Anunziata · Andrea R. Beltramone**

Received: 10 December 2013 / Accepted: 16 February 2014 / Published online: 5 March 2014


**Abstract** A series of Ti modified SBA-16 supports and their respective Ir-catalysts were prepared and characterized to study the effect of support preparation method on the dispersion of iridium and on the characteristics of Ir surface species. Two methods of incorporation of titania were tested: the sol–gel method in order to obtain Ti as heteroatom and incipient wetness impregnation to obtain Ti as $TiO_2$ (anatase phase). The results show that supports with different Ti species and dispersion can be obtained. The final catalyst was characterized at different preparation stages by XRD, elemental analysis and BET. The presence of Ti as $Ti^{4+}$ in the nanostructure of SBA and as $TiO_2$ (anatase phase) was analyzed by UV–Vis–DRS and Raman spectroscopy. The iridium oxidation sate upon Ti-containing SBA-16 was studied by XPS, EDX, TEM and XRD, arriving at the good proportion of $Ir^0$. $H_2$ chemisorption and TEM characterization for Ti-SBA-16 indicated that Ir particle size was lower than anatase/SBA-16. The catalyst that we synthesized had good activity measured in tetralin hydrogenation in presence of quinoline at mild conditions. The experimental data were quantitatively represented by a modified Langmuir–Hinshelwood-type rate equation. The preliminary results show these materials as promising catalysts for HDS/HDN reactions.

B. C. Ledesma · V. A. Vallés · L. P. Rivoira · M. L. Martínez · O. A. Anunziata · A. R. Beltramone (✉)
Centro de Investigación en Nanociencia y Nanotecnología (NANOTEC), Facultad Regional Córdoba, Universidad Tecnológica Nacional, Maestro López y Cruz Roja Argentina, 5016 Córdoba, Argentina
e-mail: abeltramone@scdt.frc.utn.edu.ar

**Keywords** Iridium-containing SBA-16 · Titanium-modified SBA-16 · Ti incorporation method · Hydrogenation · Inhibition · Reaction kinetics

## 1 Introduction

Catalytic hydrotreating (HDT) is one of the major processes in the petroleum refining industry. The HDT process is applied to the treatment of a wide variety of refinery streams, such as straight-run distillates, vacuum gas oils [fluidized catalytic cracking (FCC) feed], atmospheric and vacuum residua, light cycle oil, FCC naphtha and lube oils, among others. More stringent environmental requirements and interest in the upgrading of heavy residual fractions have stimulated increasing attention on both hydrodenitrogenation (HDN) and hydrodesulfurization (HDS) processes. It has long been recognized that HDN is more difficult and more demanding than HDS, requiring more severe reaction conditions. However, HDN has historically aroused little concern to refiners because the quantities of nitrogen compounds in conventional petroleum feedstocks were relatively small. This situation is changing due to the need for processing lower quality crude. Heavier fuels require the removal of more nitrogen in order to reduce $NO_x$ emissions, to avoid poisoning of acidic catalysts, and to meet specifications of marketable products. In the oil industry, HDN is performed using either Ni–Mo–S/$Al_2O_3$ or Co–Mo–S/$Al_2O_3$ as catalysts. The development of new catalysts that are selective to C–N cleavage and the understanding of their catalytic behavior has been an important goal over the last investigations.

Otherwise, the sulfur and nitrogen compounds found in synthetic feedstock and heavy petroleum fractions can strongly inhibit hydroprocessing reactions through competitive

adsorption. The presence of these species even at low concentrations may limit the catalytic activity observed and also require the use of higher pressures and temperatures to obtain desired conversions. Therefore, the need for more active catalysts is crucial in this process. The development of highly active and selective HDT catalysts is one of the most pressing problems facing the petroleum industry.

Noble metal-based catalysts are an interesting alternative, since they have high activity for hydrogenation of aromatic hydrocarbons, and the process can then be carried out at low temperature and pressure. The metal function is usually provided by Pt and/or Pd but it has been shown that Ir, Ru and Rh also have exceptional activity and selectivity for the target reaction of hydrogenation [1–3]. Some alumina-supported transition metal catalysts possessed much higher HDN and HDS activity than a conventional NiMo system [4–8]. For example: Rh, Ir, Ru and Pt supported on silica or alumina are known to catalyze effectively the nitrogen removal from methylamine, quinoline or pyridine also in the reduced state [9]. It should be noted that studies devoted exclusively to monometallic Ir catalysts in relation to HDT are very rare [10–12]. More often, studies are concerned with comparison of monometallic Ir and Pt catalysts [13–17]. However, the bulk of those articles have studied Ir sulfide together with a series of other noble metal sulfides. The Ir catalysts have often been used in the form of sulfides, while in about 20 % of studies they have been reduced to the metal. We found in the literature that the HDN activity of an alumina-supported Ir catalyst during the parallel HDN/HDS reaction of pyridine and thiophene was markedly higher than the activity of a Pt catalyst and that modification of a NiMoP/alumina catalyst by 0.5 % Ir increased C–N bond hydrogenolytic activity two times [18]. Factors such as the effect of catalyst preparation and metal dispersion have often been studied in connection with this process [19–22]. The results obtained in all these studies suggest that Ir could be an efficient active phase for the transformation of aromatics to saturated compounds and efficient for sulfur and nitrogen removal, either by itself or as a promoter of conventional catalysts. However, the data about the effects of Ir dispersion in different supports in hydrogenation reactions are not available at present in the literature. The pore structure of the support can affect the metal dispersion. The metal particle size of supported metal catalysts is an important factor affecting the catalytic behavior.

Transition metals in mesoporous structures have excellent potential for use in HDT reactions and they are more active than commercial Ni–Mo catalysts for nitrogen removal. Different authors [23–26], have demonstrated that a substantially better dispersion of Me is obtained by incorporation of $TiO_2$ as anatase by post-synthetic treatment, improving the catalytic performance. Klimova and co-authors [26] observed that the post-synthetic incorporation of Ti into MCM-41 by chemical grafting or incipient wetness impregnation allows obtaining new Ti-containing supports with ordered pore structure and attractive textural properties. They observed clear differences in the characteristics of Mo surface species in Mo/Ti-MCM-41 catalysts, when the incorporation of the Ti to the support took place during the hydrothermal synthesis of the MCM-41 support (Ti–MCM–S) or by post-synthetic treatment. In the latter case, a substantially better dispersion of Mo was obtained.

$TiO_2$/SBA-15 hybrid materials prepared via post-synthetic methods showed promising features as supports for NiMo catalysts highly active in deep HDS of 4,6-dimethyldibenzothiophene [25]. The authors used the grafting-precipitation method, which promotes the formation of larger $TiO_2$ anatase crystals at lower titania loadings, resulting in active catalysts for HDS. In the NiMo catalysts supported on SBA-15 materials, the dispersion of Ni and Mo oxide species increased with $TiO_2$ loading in the support. Catalytic activity test in 4,6-dimethyldibenzothiophene HDS showed that modification of SBA-15 supports with Ti species significantly improved the performance of NiMo catalysts in HDS of refractory dibenzothiophenes. The activity observed for the NiMo catalysts is closely related to the metallic species (Mo and Ni) dispersion on the support surface. This happens as a result of combining the good textural properties of the SBA-15 mesoporous molecular sieve with the high intrinsic activity that the presence of $TiO_2$ nanoparticles offers to the NiMo based HDS catalysts [24, 25]. Fierro and co-authors [27] successfully used CoMo/Ti-SBA-15 catalysts for dibenzothiophene desulfurization, but the information on SBA-16 support is scarce or inexistent.

Purely siliceous SBA-16 (*Im*3*m*) was selected as a parent material to be modified with titania because of its attractive three-dimensional mesoporous structure, which consists of large spherical cavities arranged in a body-centered cubic array and connected through smaller mesoporous openings along the (111) directions [28]. Nevertheless, SBA-16 has been considered suitable for catalyst supports because its super-large cage, high surface area, high thermal stability and, especially, three-dimensional channel connectivity, which provides more favorable mass transfer kinetics than the unidirectional pore system of other hexagonal mesoporous phases [29].

We recently reported a good performance of this catalyst in HDT processes [30].

In this paper, we describe the preparation of new mesoporous catalytic materials based on Ti-containing SBA-16, with highly and homogeneously dispersed particles of metallic iridium ($Ir^0$). To study its effect on the dispersion of transition metal, titanium was incorporated as $TiO_2$ by

post synthesis, and will be compared to that obtained with Ti-mesoporous, where Ti was incorporated during sol–gel synthesis.

The aim of the present work is to study the effect of the preparation method of titania-modified SBA-16 supports and Ti and $TiO_2$ loading on the dispersion of titania, the characteristics of the iridium supported species, and the performance of the catalysts obtained in the hydrogenation of tetralin in the presence of quinoline at mild conditions in a batch reactor. Langmuir–Hinshelwood-type rate equations were used to describe reaction kinetics with physically meaningful and well-identified parameter values.

## 2 Experimental

### 2.1 Synthesis of Si-SBA-16

Mesoporous silica materials with cubic *Im*3*m* structure were synthesized according to the procedure described by [31]. Briefly, poly (alkylene oxide)-type triblock copolymers F127 (EO106PO70EO106, MW 5 12600) were dissolved in aqueous HCl solution. Tetraethyl orthosilicate was added to the solution at 35 °C under continuous stirring during 15 min at that temperature. The molar composition of the mixture was as follows: F127/TEOS/HCl/$H_2O$ = 0.004/1/4/130. This mixture was kept under static conditions in an oven for 6 h at the same temperature. Subsequently, the mixture was placed in an oven at 50 °C, over a period of 20 h; afterwards the temperature of furnace was increased to 80 °C for aging during 20 h. After that, the solid product was recovered by filtration and dried at 100 °C. The Si-SBA-16 sample was immersed in ethanol reflux for 6 h, to extract the surfactant; it was then calcined at 550 °C in air for 6 h. The material obtained was identified as SBA-16.

### 2.2 Synthesis of $TiO_2$-SBA-16

The preparation process of $TiO_2$/SBA-16 was as follows: the as-synthesized SBA-16 was dried in oven at 80 °C for 4 h. Then, 0.5 g of dried sample was dispersed in a solution containing 2 mL of titanium tetrabutylorthotitanate and 5 mL of ethanol. The mixture was stirred at 60 °C for 8 h in order to evaporate the solvent. After that, the hybrid products were dried in a rotator evaporator in vacuum at 80 °C and calcined in air at 550 °C, with a heating rate of 5 °C/min for 4 h. The material obtained was denoted as $TiO_2$/SBA-16.

### 2.3 Synthesis of Ti-SBA-16

Mesoporous cage-like material SBA-16 was synthesized according to the procedure described previously [31]. Pluronic F127 (EO106PO70EO106) was used as the template. The template was completely dissolved in a solution of distilled water and concentrated hydrochloric acid (37 wt%). The solution was further stirred at 35 °C for 4.5 h. TEOS was used as the silica source under acidic synthesis conditions. TEOS was added dropwise to the solution with stirring at 35 °C during 4.5 h. Tetraethylorthotitanate dissolved in 10 mL of ethanol was added slowly and the solution was then reposed for another 20 h without stirring. The resulting suspension was transferred to the PP bottle. The bottle was placed under static conditions at 80 °C for 24 h. Subsequently, the precipitated solid was isolated by filtration, washed with copious amounts of water and dried overnight at 50 °C. This powdered sample was desorbed on $N_2$ flow at 500 °C for 5 h, and calcined on air at 500 °C for 5 h. The mesoporous cage-like material SBA-16 was finally obtained. The material was denoted as Ti-SBA-16 with Si/Ti ratio = 20.

### 2.4 Synthesis of Ir/Ti-Containing Mesoporous Support

We concentrate here on the direct incorporation of iridium by wetness impregnation using the calcined form of Ti-mesoporous support, followed by thermal treatment and reduction under hydrogen. We use iridium acetylacetonate (Aldrich 99.9 % $Ir(Acac)_3$) as source of Ir, employing ethanol as solvent, due to its very low solubility in water. The obtained powder was then dried at 80 °C overnight, and desorbed in inert atmosphere (nitrogen flow of 20 mL/min) from 25 °C to 200 °C with a slope of 10 °C/min and kept at this temperature during 5 h, after that, the temperature was increased to 470 °C with a slope of 10 °C/min, kept 5 h at that temperature. Then the samples were calcined at 500 °C for 5 h. Thermal programmed desorption under inert atmosphere is due to the organic nature of Ir source. If the first elimination of Acac is doing under oxidative atmosphere, the possibility of generation of larger oxide iridium cluster is greater. Under $N_2$ flow and controlled temperature desorption, the organic component of the Ir source elimination is endothermic and not oxidative, avoiding in part, the migration and agglomeration of Ir and specially IrO nano crystallites. On the other hand, desorption under inert atmosphere also avoid the possible leaching of Ti by the acid nature of the oxidative elimination of Acac. After this, we activate in muffle to eliminate some of carbon coke species from polymerized organic component of Ir source. Due to iridium is active for the reaction in its metallic state it was reduced in $H_2$ flow of 20 mL/min at 470 °C using the same procedure described above. The iridium load was 1 wt% and the materials obtained were identified as Ir/SBA-16, Ir/$TiO_2$-SBA-16 and Ir/Ti-SBA-16.

### 2.5 Characterization of the Catalysts

The XRD patterns were collected by using a continuous scan mode with a scan speed of 0.02° (2θ)/min. XRD patterns were recorded in the Philips X'Pert PRO PANalytical diffractometer, operating with Cu Kα X-ray radiation (X-ray generator current and voltage set at 40 mA and 45 kV), using small divergence and scattering slits of 1/32 mm and a goniometer speed of 1.2° (2θ)/min. The scanning range was set between 0.5° and 5°. The sample was crushed previously and placed in an aluminum sample holder. XRD data were also recorded in an interval of 40°–50° 2θ which corresponds to the hkl region of the metal (1 1 1) reflection. The breadth of this line (full width at half height) allowed a first estimation of the average metal particle size by use of the Scherrer relation [32], considering contributions from particle stress and instrumental broadening to be negligible. The validity of this hypothesis is justified by the similar values found for the average metal particle size from XRD and $H_2$ chemisorption and transmission electron microscopy (TEM). Elemental analysis was performed by inductively coupled plasma-atomic emission spectroscopy (VISTA-MPX) operated with high frequency emission power of 1.5 kW and plasma airflow of 12.0 L/min. The surface area was determined by the BET method using a Micromeritics Chemisorb 2720 apparatus, equipped with a TCD detector. Hydrogen chemisorption characterization was performed in a Chemisorb 2720 Micromeritics, measured at temperature pulses and at atmospheric pressure. The samples were previously treated and reduced. For the hydrogen chemisorption, the catalyst (0.5 g) was in situ reduced by $H_2$ (30 mL/min) at 400 °C for 2 h and purged by $N_2$ (25 mL/min) at 400 °C for an additional 0.5 h. The samples were cooled to 22 °C and titrated by $H_2$ pulses in a stream of $N_2$ until constant output TCD signal indicated saturation. The mean diameter of the Ir particles was estimated on the simple assumption of a stoichiometric value of 2 H/Ir and a spherical shape of the metal particles. The accuracy to the results is typically better than ±1.5 % with ±0.5 % reproducibility. UV–Vis diffuse reflectance spectroscopy (UV–Vis–DRS) was used to evaluate the relative distribution of octahedrally- to tetrahedrally-coordinated Ti species in the samples. The spectra were recorded with a Perkin Elmer Lamba 650 spectrophotometer equipped with a diffuse reflectance accessory. Raman spectrum was obtained from an InVia Reflex Raman microscope and spectrometer using a 532 nm diode laser excitation. X-ray Photoelectron Spectra (XPS) were obtained on a MicrotechMultilb 3000 spectrometer, equipped with a hemispherical electron analyzer and Mg Kα ($h\nu = 1{,}253.6$ eV) photon source. An estimated error of ±0.1 eV can be assumed for all measurements. Intensities of the peaks were calculated from the respective peak areas after background subtraction and spectrum fitting by a combination of Gaussian/Lorentzian functions. The relative surface atomic ratios were determined from the corresponding peak intensities, corrected with tabulated sensitivity factors, with a precision of ±7 %. Energy-dispersive X-ray (EDX) analysis were coupled to the scanning electron microscopy LEO Mod. 440 equipment. Ir-particle sizes were evaluated from TEM images recorded in a JEOL 2100F microscope operated with an accelerating voltage of 200 kV and equipped with a field emission electron gun providing a point resolution of 0.19 nm and checked by XRD technique using the Scherrer equation.

### 2.6 Catalytic Activity

The catalytic activity was measured in a 4563Parr reactor. Experiments were undertaken at predetermined conditions (250 °C, 15 atm of hydrogen pressure, 360 rpm and particle diameter <0.64 mm) where no significant mass-transfer effects were expected. The feed consisted of 50 mL of 5 % v/v of tetralin (98.5 % FLUKA) in dodecane in the presence of 100 ppm of N as quinoline. The results were compared with those of a typical HDT catalyst as $NiMo/Al_2O_3$ Criterion DN200. The products were analysed with a HP 5890 Series II GC and HP-5 column.

## 3 Results and Discussion

### 3.1 Characterization of the Catalysts

#### *3.1.1 XRD*

For the determination of the structure and symmetry of the materials, XRD patterns were analysed. SBA-16 with cubic *Im*3*m* structure is a body-centred-cubic arrangement of cages with eight apertures to the nearest neighbours. The unit-cell parameter, $a_0$, of the crystallographic structure was obtained by solving the following equation depending on the type of space group: $a_0 = d_{hkl} \cdot \sqrt{(Q_{hkl})}$, where $Q_{hkl}$ is: $Q_{hkl} = h^2 + k^2 + l^2$, for a cubic space group like the cubic body centred (*Im*3*m*) SBA-16. A typical X-ray diffractogram of SBA-16 is expected to present peaks at $2\theta < 3°$, corresponding to an *Im*3*m* cubic structure [33, 34]; however, quite often, just the first two peaks are clearly detected [35, 36]. Figures 1 and 2 show the X-ray diffractograms of the SBA-16 and Ir-titanium modified SBA-16. The XRD pattern of calcined SBA-16 sample shows a very strong (1 1 0) reflection (1.2° 2θ) of the cubic *Im*3*m* structure and two small shoulders of the (2 0 0) and (2 1 1) reflections (1.7° and 1.92° 2θ, respectively). All these reflections yield an $a_0$ value of 12.16 nm (Table 1), confirming that the measured structure is indeed the *Im*3*m* structure [37, 38].

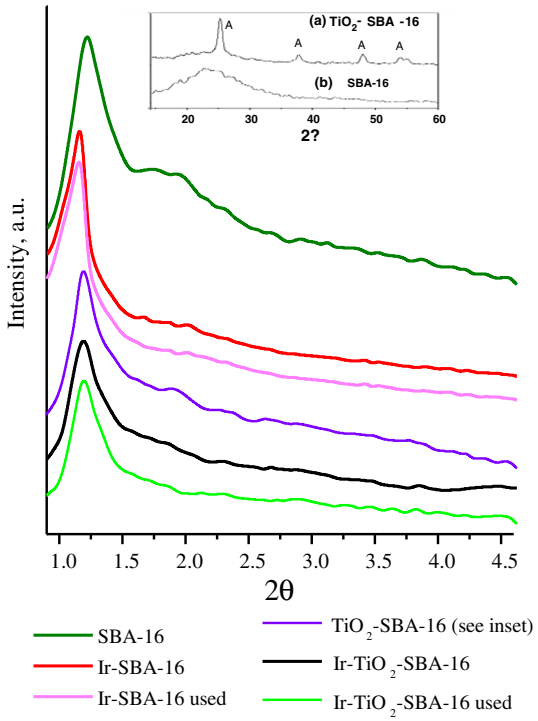


**Fig. 1** XRD pattern of $TiO_2$-modified SBA-16 synthesized samples

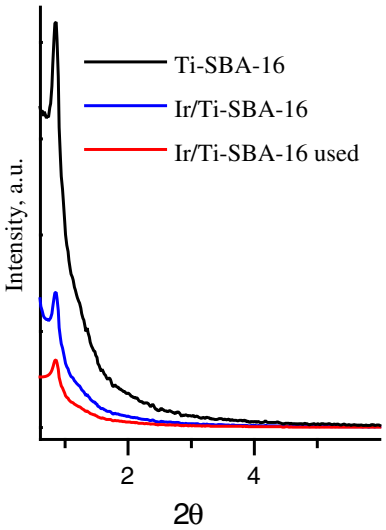


**Fig. 2** XRD pattern of Ti-modified SBA-16 synthesized samples

Figure 1 shows the wide-angle XRD patterns of $TiO_2$/SBA-16. The wide-angle XRD pattern of $TiO_2$/SBA-16 shows full sets of peaks corresponding to the pure anatase phase, in addition to the wide line of amorphous silica centered at $2\theta = 23°$. The XRD peaks are relatively broad due to the small size of the $TiO_2$ nanoparticles, indicating that major of $TiO_2$ particles are formed inside SBA-16 during the inclusion process. The $TiO_2$ nanocrystal size

**Table 1** Physicochemical and structural properties of the supports and catalysts

| | $a_0$ (nm) | Area ($m^2$/g) | Ir (wt%)[a] | D (%)[b] | Average size of Ir metallic clusters (nm) |
|---|---|---|---|---|---|
| SBA-16 | 12.16 | 870 | – | – | – |
| Ir/SBA-16 | 12.40 | 560 | 0.92 | 48 | 2.40[b]–2.60[c,d] |
| Ir/$TiO_2$-SBA-16 | 12.70 | 450 | 1.02 | 60 | 2.11[d]–2.50[b] |
| Ir/Ti-SBA-16 | 12.60 | 520 | 1.04 | 85 | 1.94[d]–2.30[b] |
| Ir/$Al_2O_3$ | – | 162 | 0.99 | 33 | 3.90[b]–4.30[c] |

[a] ICP-AES

[b] D (%) = percentage metal dispersion obtained from hydrogen chemisorption

[c] XRD

[d] TEM

calculated according to the Scherrer diffraction formula ($d = \kappa\lambda/\beta \cos\theta$) was about 6 nm, which is consistent with the pore diameter of SBA-16 (between 6 and 9 nm). This indicates that the limited pore channels of SBA-16 restricted the growth of $TiO_2$ nanoparticles. In the case of Ti-SBA-16 (Fig. 2), the characteristic signals at 1.2° 2θ (1 1 0) reflection and two poorly-resolved weak peaks at 1.7° and 1.9° due to (2 0 0) and (2 1 1) shifted to lower $2\theta$ values evidencing an increase in the unit cell parameters ($a$ for the cubic Ti-SBA-16) and substitution of $Ti^{4+}$ for $Si^{4+}$ in the framework location of mesoporous silica (Fig. 2; Table 1).

The diffraction signal at corresponding Miller index of SBA-16 indicates that the ordered mesoporous structure was preserved after the incorporation of iridium. Table 1 shows the $a_0$ values for all the samples. In the Figures, we also can observe, a pattern for used Ir/mesoporous (after the catalytic test). This fact demonstrates that the structure remains unalterable, even after three reaction cycles.

The textural and structural properties of Ir catalysts supported on Ti-containing SBA-16 materials are given in Table 1. The content of iridium in the catalysts was determined by ICP and the iridium dispersion in the reduced catalysts was determined by pulse $H_2$ adsorption at 22 °C and TEM (Table 1). The lower Ir crystal size was observed in Ti-SBA-16 support, with higher dispersion, showing an agreement between the data obtained by $H_2$ chemisorptions and TEM results.

The incorporation of a metal in the structure therefore leads to a slight decrease in the surface area but the pore diameter and the mesoporous character are maintained. However, the values agree sufficiently well to allow concluding that all the metal is accessible to hydrogen, and that

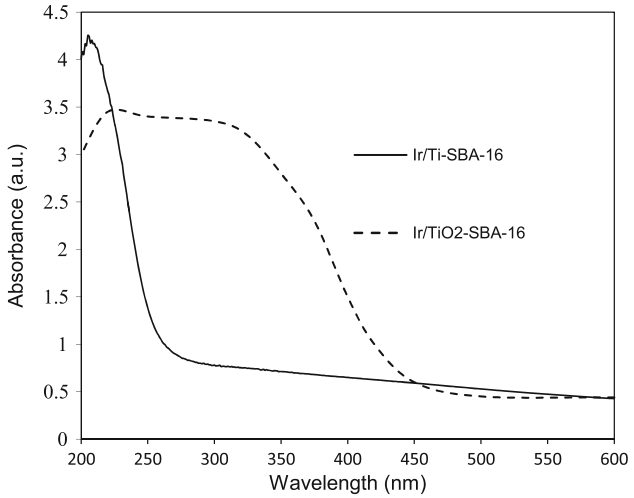


**Fig. 3** UV–Vis diffuse reflectance spectra of Ir/Ti-SBA-16 and Ir/$TiO_2$-SBA-16

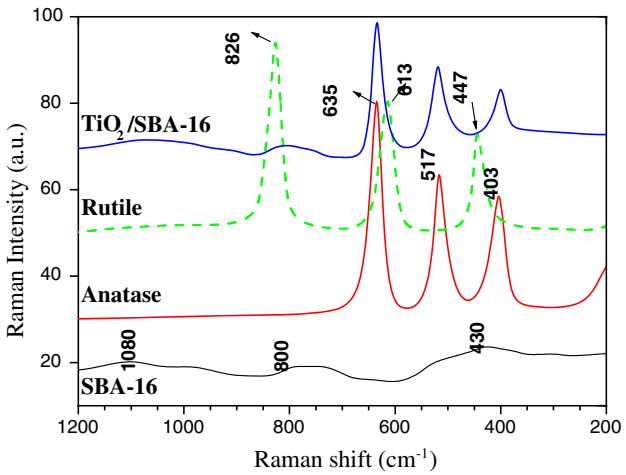


**Fig. 4** Raman spectra of SBA-16 and $TiO_2$-SBA-16

no side phases are formed. In summary, in these various iridium metal-containing systems, metal particle size depends on metal content, support, surfactant and method of incorporation. After catalytic reaction with tetralin, the metal particle size estimated from width of the X-ray diffraction line is unchanged.

### *3.1.2 UV–Vis Diffuse Reflectance Spectroscopic Analysis*

UV–Vis diffuse reflectance spectroscopy (UV–Vis–DRS) was used to study the dispersion and chemical environment of hetero-elements incorporated in silica materials. Figure 3 shows the UV–Vis–DRS spectra of Ti-SBA-16 and $TiO_2$-SBA-16 materials. The signals have the bands at 210, 240–320 and 320–400 nm, which are usually taken as a clear evidence for the isolated framework Ti(IV), octahedral coordinated Ti species, and titania (anatase) phase, respectively [39–41]. Ti-SBA-16 has the band only at 210 nm, corresponding to tetragonal titanium with Ti $(OSi)_4$ structure. The intense ligand-to-metal charge-transfer transition band at $\sim$200 nm ($O^{2-} \rightarrow Ti^{4+}$), which could be attributed to mono-atomically dispersed $Ti^{4+}$ ions in tetra-coordinated geometry, clearly indicates that most of Ti ions are isolated and in tetrahedral (Td) coordination [41]. The absence of an absorption band characteristic of extra-framework titanium in the range of 330–400 nm suggests that most of the Ti ions occupy sites in silica framework. The results indicated that the Ti species introduced are well-dispersed in the SBA-16 mesoporous framework, in good agreement with what is determined from the wide-angle XRD patterns.

Figure 3 also shows the UV–Vis spectra of $TiO_2$/SBA-16. A significant increase in the absorption at wavelengths shorter than 400 nm can be assigned to the intrinsic band gap absorption of pure anatase $TiO_2$. The absorption edge of the $TiO_2$/SBA-16 sample is found to be a wavelength range shorter than that of the bulk anatase $TiO_2$ sample [39, 41]. The blue shift is ascribed to the decrease in crystallite size. The pore channels of SBA-16 provide a size confinement for $TiO_2$ particles with a maximum size of about 6 nm.

## 3.2 Raman

Raman analysis of the powder treated at 450 °C for 2 h is shown in Fig. 4, where the spectrum exhibits well-defined bands at 635, 517 and 403 $cm^{-1}$ which are the characteristic bands for pure anatase [42]. Rutile bands at 826, 613 and 447 $cm^{-1}$ [43] are clearly shown in the spectrum of the pure sample, whereas in the Raman spectra of anatase-supported sample ($TiO_2$-SBA-16), the characteristics signals of anatase upon the background of SBA-16 are detected. Thus, the Raman analysis allowed us to support the incorporation of anatase phase, rather than rutile phase, forming nano-crystalline clusters with SBA-16 as support.

### *3.2.1 XPS*

Iridium 4f signal of Ir nanoparticles dispersed in Ir/Ti-SBA-16 and Ir/$TiO_2$-SBA-16 is shown in Fig. 5. One can notice a component corresponding to Ir(0) or Ir–Ir bonds (Ir7/2 at 61.2 eV and Ir5/2 at 64.5 eV, solid line) and an Ir–O (dot line) contribution at 62.5 and 65.5 eV; a slight shift is observed towards a higher BE for iridium species by their interaction with the support: 62.0 eV for Ir–O and 61.0 eV for $Ir^0$ [44, 45]. In the case of Ti-SBA-16 (Fig. 5A), the peak area analysis makes a contribution of 81 % $Ir^0$ and 19 % Ir–O. It can be observed that the

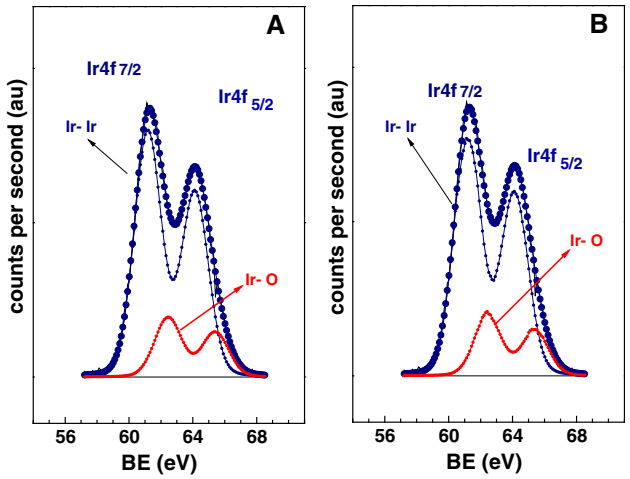


**Fig. 5** Core level Ir 4f XPS spectra of Ir/Ti-SBA-16 (**a**) and Ir/$TiO_2$-SBA-16 (**b**)

**Table 2** Characteristics of Ir and Ti species obtained by XPS and EDX of Ir/Ti-SBA-16 and Ir/$TiO_2$-SBA-16 catalysts

| Sample | XPS | | | EDX |
|---|---|---|---|---|
| | $Ir4f_{7/2}$ | Ti $2p_{3/2}$ | Atomic Ratio | |
| Ir/Ti-SBA-16 | 61.2 (81) $Ir^0$ | $Ti2p_{3/2}$ = 459.4 | Si/Ir = 270 | Si/Ti = 23.7 Si/Ir = 14.2 |
| | 62.5 (19) Ir–O | | Si/Ti = 454 | |
| Ir/$TiO_2$-SBA-16 | 61.2 (79) $Ir^0$ | $Ti2p_{3/2}$ = 458.5 | Si/Ir = 265 | Si/Ti = 26.0 Si/Ir = 14.4 |
| | 62.5 (21) Ir–O | | Si/Ti = 360 | |

nanoparticles in Ti-SBA-16 show a significant contribution from the Ir–Ir component character, in agreement with XRD and TEM results. For $TiO_2$-SBA-16 sample, the contribution of $Ir^0$ was 79 % and Ir–O was 21 %, according to the data shown in Fig. 5b and Table 2, very close to the values of Ir state on Ti-SBA-16 sample.

The reduction of IrO to $Ir^0$ was carried out at 470 °C under $H_2$ flow for all the samples. We have found the low temperature peak at 280 °*C* due to the reduction of well-dispersed Ir species (over Ti-SBA-16 and $TiO_2$/SBA-16) and a peak at 450 °C, which probably corresponds to the presence of larger IrOx particles that interact strongly with SBA-16 support [46–49].

Analysis of Ti species was also performed by XPS (Table 2). According to the literature [50], Ti–O–Si heterolinkages (in $TiO_2$–$SiO_2$) can be easily detected as a variation in the core level binding energies in XPS spectra. For example, difference in the Ti $2p_{3/2}$ core-level BE is ~8 eV between $Ti^0$ in metal and $Ti^{4+}$ state in $Na_2TiF_6$ or $ZrTiO_4$ [50]. Among oxides, however, the difference is not so pronounced and in some cases the identification of Ti valence states in different titanates becomes conjectural; in this case, according to XPS spectra (not shown), Ti appears as $Ti^{4+}$ (–$O_4$–) $Ti_{2p3/2}$ = 459.4 eV (Table 2), due to the isomorphous Si substitution in Ir/Ti-SBA-16. In this way, for Ir/$TiO_2$-SBA-16 sample, the $Ti_{2p3/2}$ = 458.5 eV agrees with literature data ($TiO_2$ as anatase, $Ti2p_{3/2}$ = 458.6 eV [49]). Thus, in agreement with the data obtained by UV–Vis, XPS data on Ti indicate that it is incorporated in the mesoporous nanostructure of SBA-16, as anatase phase in one case and as $Ti^{4+}$ isolated ions in Td coordination when Ti is added in the sol–gel stage of the catalyst synthesis. Following the atomic ratio of Si/Ir (270) and Si/Ti (454) from the XPS analysis, Ti and Ir species are well dispersed in the mesoporores of SBA-16 due to the low signal observed in XPS analysis (100 Å depth). The same takes place with the noble metal employed is this work: most of it lies within the pore nanostructure. This is supported by EDX results for Si/Ti and Si/Ir in the samples (Table 2), taking account of the very low Si/Ti and Si/Ir ratios, compared with the those obtained by XPS.

### 3.3 TEM

The morphology of the support and dispersion of metallic nanoparticles over Ti-SBA-16 and $TiO_2$-SBA-16 was examined by means of TEM. The TEM images (Fig. 6) of the catalysts and their corresponding PSDs (particle size distribution) are shown in Table 1 and Fig. 7, respectively. The particle size distribution ranging from 0.5 to 6 nm indicate that catalyst metal particles were mainly present inside the pores, the mean particle diameter was found to be close to 2 nm in both cases indicating that most of the particles reside inside of the pore system. The mean particle diameter (1.94 nm) of Ir/Ti-SBA-16 catalyst prepared by direct incorporation of Ti by sol–gel method was found to be slightly smaller than that of the catalyst prepared by impregnation method. The direct incorporation method also gave better dispersion of metal particles (Table 1).

### 3.4 Catalytic Activity

The catalytic activity of the synthesized samples was compared with that of a commercial NiMo/$Al_2O_3$ presulfided catalyst and commercial Ir/$Al_2O_3$, using Topsoe M-80T γ-alumina and with the same % of iridium, prepared with the same procedure as the other samples, as indicated in the experimental section.

The hydrogenation reactions of tetralin were carried out at 250 °C and 15 atm in the presence of traces of quinoline. The

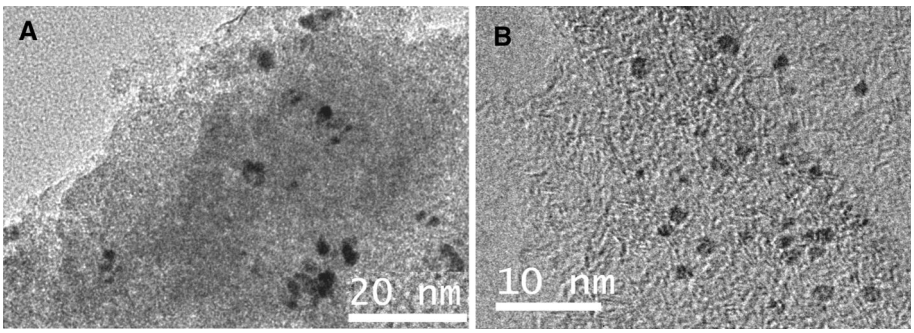


**Fig. 6** TEM: Image of Ir/$TiO_2$-SBA-16 (**a**) and Ir/Ti-SBA-16 (**b**)

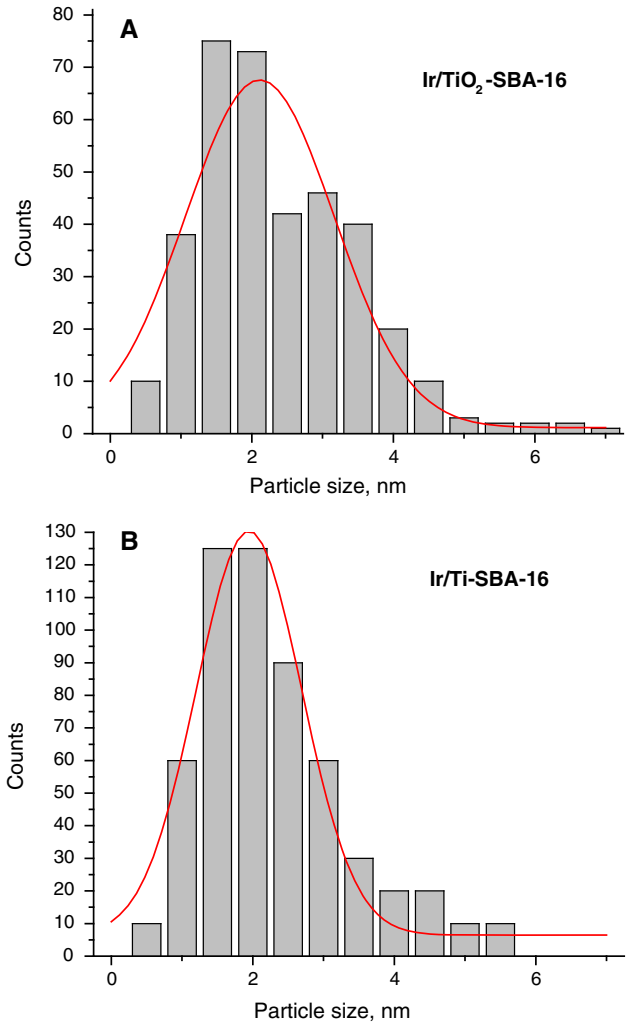


**Fig. 7** Histograms of PSDs measured from full images of Ir/$TiO_2$-SBA-16 (**a**) and Ir/Ti-SBA-16 (**b**) partially shown in Fig. 6

major products were *trans*-decalin and *cis*-decalin, the presence of naphthalene was negligible since the experiments were performed far below the thermodynamic equilibrium. Decalins appeared to be unreactive under these conditions.

In order to study the behavior of the samples, computation of kinetic parameters can be useful to shed further light on this issue since the data will be used to provide a better value for the constraints used to obtain the rate constants in the model. Generalized Langmuir–Hinshelwood rate equation can represent the behavior of the different catalysts on the tetralin hydrogenation.

### 3.5 Kinetic Calculations

Tetralin hydrogenation rate constants based on the rate of tetralin disappearance were calculated using the integral method. The slope and the correlation coefficient were calculated via least-squares fitting. In all cases the correlation coefficients obtained were higher than 0.92. *Trans*-decalin and *cis*-decalin were observed as the main products of the tetralin hydrogenation reaction (99 %). The semi-empirical kinetic model proposed is the generalized Langmuir–Hinshelwood model for hydrogenation; for tetralin hydrogenation, the reaction rate is given by:

$$r_{TL} = \frac{k K_{TL} C_{TL}}{1 + K_{TL} C_{TL}} x \frac{K_{H_2} C_{H_2}}{1 + K_{H_2} C_{H_2}}, \quad (1)$$

where $r_{TL}$ is the tetralin conversion to decalin rate, $C_{TL}$ is tetralin concentration and $C_{H2}$ is hydrogen concentration, $k$ is the rate constant and $K$ is the adsorption equilibrium constant of the individual compounds. Under our experimental conditions, $K_{H2}C_{H2} \gg 1$, therefore, this kinetic equation could be simplified as:

$$r_{TL} = \frac{k K_{TL} C_{TL}}{1 + K_{TL} C_{TL}} \quad (2)$$

expressing $kK_{TL}$ as $k_{TL}$. The values obtained for $k_{TL}$ at 250 °C using the integral method already described are shown in Table 3. These values will be used as a reference for the results obtained in the experiments where this reaction is inhibited by nitrogen as quinoline.

### 3.6 Control of the Kinetic Regime

A set of experiments was performed to check the absence of intraparticle and interphase mass transfer limitations. Different sizes of catalyst particles (0.2, 0.4, 0.6, 0.8 mm)

**Table 3** Kinetic constants for the different samples derived from kinetic analysis

| Samples | Kinetic constant $K_{TL}$ (L/min mmol) | Adsorption quinoline constant K (L/mmol) |
|---|---|---|
| Ir/Ti-SBA-16 | 0.0160 | 85 |
| Ir/$TiO_2$-SBA-16 | 0.0098 | 120 |
| Ir/SBA-16 | 0.0073 | 147 |
| Ir/$Al_2O_3$ | 0.0035 | 90 |
| NiMo/$Al_2O_3$ (Criterion DN200) | 0.0014 | 80 |

were tested; the results indicated that, in all cases a kinetic regime was established.

### 3.7 Kinetic Model for Tetralin Inhibition by Nitrogen

The hydrogenation of tetralin reaction was carried out at 250 °C and 15 atm in the presence of quinoline (concentration equivalent to 100 ppm as nitrogen). The inhibiting effect in the tetralin hydrogenation was studied according to LaVopa and Satterfield [51], and the following equation was proposed:

$$r_{TL} = \frac{k_{TL} C_{TL}}{1 + \sum K_i C_i}, \tag{3}$$

where $r_{TL}$ is the pseudo-first-order rate constant for the reaction inhibited by nitrogen compounds, *Ki* is the apparent nitrogen compound adsorption equilibrium constant (L/mmol) representing the behavior of the nitrogen compound that contributes to the inhibition, and *Ci* is the initial quinoline concentration (mmol/L). The results of these experiments (Fig. 8) were fitted according to Eq. (3), with correlation coefficients ($R^2$) better than 0.98 in all cases. The excellent representation of the experimental results by the proposed rate equation implies that the inhibition effect is approximately constant during each test. The inhibiting strength does not seem to be affected by the conversion of the parent nitrogen compound. This behavior suggests that the coverage of the available active sites by nitrogen compounds is established in the early stages of the reaction and remains nearly constant throughout the experiment, probably due to the slow desorption kinetics of these compounds [52, 53]. The parameter estimation of the kinetic model was performed with the Powell version of the Levenberg–Marquardt algorithm. The differential equation was solved using the EPISODE package of Scientist®. The objective function (Eq. 4) was the sum of the squares of the differences between experimental and calculated yield of decalin versus time of the reaction, for each catalyst (Fig. 8).

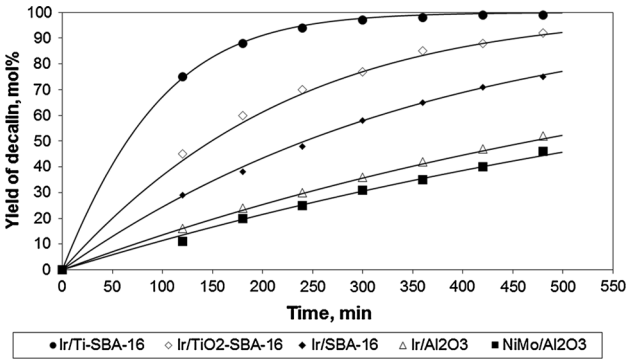


**Fig. 8** Kinetics of the hydrogenation of tetralin at T = 250 °C, P = 15 atm, 360 rpm. 100 ppm of nitrogen as quinoline was added to the feed. The lines were obtained by fitting the kinetic curves derived from the model to the experimental data ($F = 1.49^{-4}$)

$$F = \sum_{1}^{n} \left(y_{\exp} - y_{cal}\right)^2. \tag{4}$$

The catalytic results reveal the good performance of these monometallic Ti-modified catalysts at low temperatures, where high conversions and high yields of hydrogenation products are obtained, improving the behavior displayed by the commercial catalyst. It should be noted that these catalysts need lower contact times and hydrogen/tetralin molar ratios than those of the NiMo catalyst, thus reducing the cost of the process if used in future industrial applications.

According to the catalytic test, the Ir/Ti-SBA-16 synthesized sample was the most active catalyst in this reaction taking account of the kinetic constant values (Table 3). Differences in activity can results from the better iridium dispersion obtained on Ti-SBA-16 used as support.

The major products were *trans*-decalin and *cis*-decalin, we also observed traces of naphthalene. *Trans*-decalin was the product with the highest initial selectivity, followed by *cis*-decalin. The *trans* isomer is expected to be favored based on thermodynamic calculations. In Fig. 9 we can observe that the *trans*/*cis*-decalin ratio is almost constant for the bunch of catalyst tested in this study, with the exception of NiMo catalyst, in which the ratio clearly increases with TL conversion, this in agreement with a previous study using industrial conditions (higher temperatures and pressures) [54]. Ti-SBA-16 presented the lower *trans*/*cis* ratio, what is good since *trans*/*cis* ratio is important as previous studies [55] have shown that only the *cis* form of decalin can be ring-opened without cracking on an acid catalyst.

From the results of characterization presented above, it is possible to conclude that the two methods of Ti incorporation tested in this study allowed preparation of

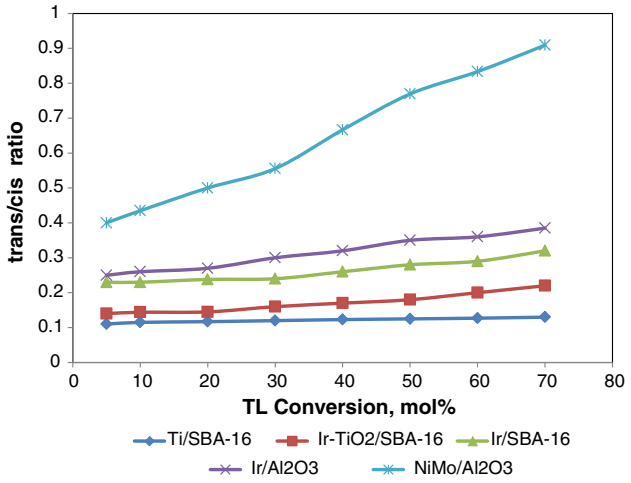


**Fig. 9** *Trans/cis* decalin ratio versus tetralin conversion

mesoporous SBA-16-type materials with relatively high Ti and/or $TiO_2$ loadings and without considerable decomposition of the initial SBA-16 structure. As reported in the literature [56], hydrothermal and grafting incorporation of titanium species leads to Ti-SBA-16 supports with highly dispersed Ti species; yet titanium loading in that case is limited by the number of reactive OH groups on the surface of the parent Si-SBA-16. However, in our case, the titania loading that could be achieved with the sol–gel method is not limited as the hydrothermal synthesis.

The appearance of anatase signals in the XRD patterns and DRS and XPS spectra of samples prepared by $TiO_2$ incipient wetness impregnation show worse iridium dispersion than with the sample prepared by sol–gel synthesis. In addition, it was found that in the samples prepared by impregnation, different Ti species are present simultaneously, such as isolated Ti species and small anatase clusters (inside the mesopore channels of SBA-16), with a very low proportion of anatase crystallites on the external surface $Si/TiO_2 = 360$ by XPS and $Si/Ti = 26$ by EDX (Table 2) corroborated by Raman results (Fig. 4).

We have obtained higher Ti loading without substantial loss of the parent SBA structure and texture. Ti particles are accessible for its interaction with the Ir active species and help the possibility of fine tuning of the characteristics of the deposited Ir-species.

Amezcua et al. [56] found that $TiO_2$ incorporation in the SBA-16 support leads to stronger interaction of Mo and Ni oxidic species with the support, providing better dispersion to the sulfided metal species. Additionally, it was found that titania enhances the reduction and sulfidation of $Mo^{6+}$ oxide species making the formation of catalytically active $MoS_2$ easier.

It seems therefore that the order of the activity was influenced by the method of incorporation of titanium on the support, which can affect the strength of the interaction with the noble metal precursor. The decreasing trend with increasing Ir cluster size is well apparent. Hydrogen chemisorption measurements over these catalysts in the reduced state have suggested that the higher activity of the samples with smaller Ir size can be explained by the higher Ir dispersion [57].

In Fig. 8, we can observe the activity of the different samples included in this study in the presence of quinoline. The activity increases as follows: $NiMo/Al_2O_3 < Ir/Al_2O_3 < Ir/SBA\text{-}16 < Ir/TiO_2\text{-}SBA\text{-}16 < Ir/Ti\text{-}SBA\text{-}16$. The inhibiting effect of nitrogen (according to the adsorption constant values) is strong at concentrations as low as 100 ppm, but Ir/Ti-SBA-16 is still more active than with commercial NiMo/alumina catalyst (i.e.TL mol% conv. obtained at the same conditions was 75 % higher at 4 h of reaction).

This maximum in catalytic activity was attributed to the formation of a noble metal active phase with an optimal cluster size and an electronic environment capable of being more nitrogen-resistant. In our case, the activity trend with the change in the Ti-containing SBA-16 support seems to be the result of two opposite effects. On the one hand, the incorporation of titanium into the support surface provides a stronger metal-support interaction, allowing better dispersion of the iridium phases. This explains an increase in tetralin conversion with Ti-loading in Ir/Ti-SBA-16 catalysts. On the other hand and when titania loading is as $TiO_2$, as in the case of $Ir/TiO_2$-SBA-16 catalyst, a support with slightly lower surface area is obtained, in which the formation of larger Ir particles and some pore plugging could be supposed.

Then, the inhibition behavior seems to be related to the strong adsorption of the specific nitrogen compound directly on the catalyst surface [58–60]. In order to elucidate that fact, adsorption constants were determined. Calculated Langmuir adsorption constants for all the samples tested are listed in the second column of Table 3, for those data obtained at 250 °C. Among these compounds, adsorption strength increased in the order of $NiMo/Al_2O_3 < Ir/Ti\text{-}SBA\text{-}16 < Ir/Al_2O_3 < Ir/TiO_2\text{-}SBA\text{-}16 < Ir/SBA\text{-}16$.

The lower nitrogen tolerance of Ir in SBA-16 as compared to Ti-SBA-16 could be explained by a stronger adsorption of nitrogen on Ir owing to a lower electron affinity. On the other hand, the lower nitrogen resistance of 1 wt%. Ir containing SBA-16 might be explained by a higher electron-deficient character of the smaller Ir particles present in Ti-SBA-16.

This would favor nitrogen tolerance due to a larger steady state active surface area in the case of the incorporation of titanium in the structure of SBA-16.

The resistance to poisoning depends, to a large extent, on the nature of the support, as well as on the size, structure

and location of the metal particles, and many points are still under discussion.

Metal-support interaction brought about an increase in the amount of electron-deficient metal sites, which improved nitrogen tolerance by reducing irreversible electrophilic adsorption and thereby reducing N-induced coke formation. Electron-deficient species in bimetallic catalysts are claimed by a number of researchers to be responsible for S and N tolerance against the electron-acceptor character of the nitrogen or sulfur [61–63].

Literature reports [56, 64] indicate that activity increases with titania loading in the support, but further increase in $TiO_2$ loading results in less active NiMo catalysts with low surface area and porosity. They show the suitable methods of incorporation of titanium into the SBA-type materials and optimum $TiO_2$ loadings for the preparation of active HDS catalysts. In our case a catalyst with high titania loading and high activity was successfully developed.

This fact is probably due to the very small Ir particle size, as evidenced by $H_2$-chemisorption and TEM, which according to Foger and Anderson [65] is significantly influenced by the support. Even slight variations in the preparation method may alter the promotion trends or the support effect trends.

Titanosilicate molecular sieves have been known to have remarkable Lewis acidity [66–69]. Srinivas et al. [69, 70] revealed that Lewis acidic $Ti^{4+}$ ions increase catalytic activity by enhancing the adsorption of the substrates. Acidity measurements (pyridine adsorption-IR and $NH_3$-TPD) reveal the presence of only weak Lewis acid sites, whose acid strength increases in the order: TS-1 < Ti-MCM-41 < amorphous $TiO_2$–$SiO_2$.

In addition, Ti-substituted mesoporous silica materials have acquired wide applications due to their moderate acidity. As reported, $TiO_2$ catalyst has much higher acidity than $TiO_2$ metal oxides alone [70–72]. That could be the reason for its better resistant to nitrogen and/or sulfur molecules than its pure silica parent.

Results show that Ti-SBA-16 prepared by ethanol solution extracting template has higher concentration of surface Si–OH groups than SBA-16 prepared by impregnation, resulting in high Ti content.

The presence of Ti-species on the surface of SBA-16 increases the strength of Ir interaction with the SBA-16-type support, leading to a more homogeneous distribution of Ir-species than on other pure silica supports tested. However, this interaction was not so strong as to result in the formation of Ir species difficult to reduce. Consequently, Ir catalysts supported on Ti-modified SBA-16 and especially Ti-SBA-16 were more resistant to N poisoning than their analogue pure silica-supported. Titania on the SBA-16 surface also increased the hydrogenation ability of the catalysts.

The catalysts shows better activity and nitrogen-tolerance than other catalysts described in the literature, which exhibited higher deactivation by sulfur [73, 74], although it is difficult to compare our results with those of other catalysts since they are tested under different experimental conditions.

## 4 Conclusions

Despite the industrial conditions that use high pressure and temperature, we are addressing here more active catalysts that function at mild conditions and in batch reactors.

The Ir/Ti-SBA-16 catalyst synthesized by us had the highest activity measured in tetralin hydrogenation at mild conditions. The good activity was correlated with higher Ir dispersion on Ti-SBA-16 nanostructured material used as a support, with higher active metal sites exposed to reactant. The kinetic model was successfully applied to the hydrogenation of tetralin in the presence of quinoline. The hydrogenation rates were useful to determine the most active catalyst. The hydrogenation rates of tetralin were lower when quinoline was present in the mixture. The inhibition was described reasonably well by Langmuir–Hinshelwood kinetic model. Adsorption strength of the inhibitors increased as follows: $NiMo/Al_2O_3$ < Ir/Ti-SBA-16 < $Ir/Al_2O_3$ < $Ir/TiO_2$-SBA-16 < Ir/SBA-16. Even when quinoline adsorption constant for NiMo was lower than for Ir/Ti-SBA-16, the last was far more active for this reaction. The nitrogen tolerance of the Ir/Ti-SBA-16 catalyst was sufficiently high to envisage use in the final stages of a refinery process producing diesel fuel of high cetane number by hydrodearomatization.

All the above allows us to conclude that the combination of the SBA-16-type mesostructured material with titania or titania oxides leads to new supports with outstanding textural properties and an appropriate interaction with Ir species, which can be useful for the preparation of HDT catalysts. Mesoporous molecular sieves modifed with Ti via sol gel-synthetic methods show, therefore, promising features as supports for Me-based HDT catalysts.

**Acknowledgments** The authors are very grateful to Drs. J.L. García Fierro, J.M Martin and H. Falcon for XPS, UV–Vis-DRS and TEM characterization performed in ICP-CSIC. Madrid. We thank to CONICET Argentina, PIP No. 112-200801-00388 (2009-2013) and MINCyT Cba. 1210/07 (2007-2013) for financial assistance.

## References

1. McVicker GB, Touvelle MS, Hudson CW, Vaughan DEW, Daage M, Hantzer S, Klein DP, Ellis ES, Cook BR, Feeley OC, Baumgartner JE (1998) Process for selectively opening

naphthenic rings. Exxon Research and Engineering Company. US Patent 5,763,731
2. Hantzer S, Touvelle MS, Chen, J (1997) Selective opening of five and six membered rings. Exxon Research and Engineering Company. International Patent WO 97/09289
3. Touvelle MS, McVicker GB, Daage M, Hantzer S, Hudson CW, Klein DP, Vaughan DEW, Ellis ES, Chen J (1997) Process for selectively opening naphtenic rings. Exxon Research and Engineering Company. International Patent WO/09290
4. Cunha D, Cruz G (2002) Appl Catal A 236:55–66
5. McVicker G, Daage M, Touvelle M, Hudson C, Klein D, Baird W, Cook B, Chen J, Hantzer S, Vaughan D, Ellis E, Feeley O (2002) J Catal 210:137–148
6. Arribas M, Concepción P, Martínez A (2004) Appl Catal A 267:111–119
7. Nylen U, Delgado JF, Järás S, Boutonnet M (2004) Appl Catal A 262:189–200
8. Frety R, da Silva P, Guenin M (1990) Appl Catal A 57:99–103
9. Dees MJ, den Hartog AJ, Ponec V (1991) Appl Catal A 72:343–360
10. Cinibulk J, Vít Z (1999) Appl Catal A 180:15–23
11. Vít Z (2007) Appl Catal A 322:142–151
12. Frety R, Da Silva PN, Guenin M (1990) Appl Catal A 57:99–103
13. Navarro R, Pawelec B, Fierro JLG, Vasudevan PT, Cambra JF, Arias PL (1996) Appl Catal A 137:269–286
14. Barbier J, Marecot P, Tifouti L, Guenin M, Frety R (1985) Appl Catal A 19:375–385
15. Matsui T, Harada M, Ichihashi Y, Bando K, Matsubayashi N, Toba M, Yoshimura Y (2005) Appl Catal A 286:249–257
16. Cowan R, Høglin M, Reinink H, Jsebaert J, Chadwick D (1998) Catal Today 45:381–384
17. Dhainaut E, Charcosset H, Cachet Ch, de Mourgues L (1982) Appl Catal A 2:75–86
18. Rocha AS, Moreno EL, da Silva GPM, Zotin JL, Faro AC Jr (2008) Catal Today 133–135:394–399
19. Dees MJ, den Hartog AJ, Ponec V (1991) Appl Catal A 72:343–360
20. Ponec V (1983) Adv Catal 32:149–214
21. Barbier J, Marecot P (1986) J Catal 102:21–28
22. Liua Z, Li J, Junaid A (2010) Catal Today 153:95–102
23. Klimova T, Gutiérrez O, Lizama L, Amezcua J (2010) J Microporous Mesoporous Mater 133:91–99
24. Lizama L, Perez M, Klimova T (2008) Zeolites and related materials: trends, targets and challenges. In: Proceedings of 4th international FEZA conference, pp 1251–1254
25. Gutiérrez-Tinoco O, Romero-Moreno K, Leocadio-Cerón E, Fuentes-Zurita G, Klimova T (2006) Revista Mexicana de Ingeniería Química 5(3):179–187
26. Amezcua JC, Lizama L, Salcedo C, Puente I, Dominguez JM, Klimova T (2005) Catal Today 107–108:578–588
27. Nava R, Ortega RA, Alonso G, Ornelas C, Pawelec B, Fierro JLG (2007) Catal Today 127:70–84
28. Cheng CF, Lin YC, Cheng HH, Chen YC (2003) Chem Phys Lett 382(56):496–501
29. Sakamoto Y, Kaneda M, Terasaki O, Zhao DY, Kim JM, Stucky G, Shin HJ, Ryoo R (2000) Nature 408:449–453
30. Balangero Bottazzi GS, Martínez ML, Gomez Costa M, Anunziata OA, Beltramone AR (2011) Appl Catal A 404(1):30–38
31. Kim TW, Ryoo R, Kruk M, Gierszal K, Jaroniec M, Kamiya S, Terasaki O (2004) J Phys Chem B 108:11480–11489
32. Imelik B, Vedrine JC. In: Imelik B, Vedrine JC (eds) (1994) Catalyst characterisation, physical techniques for solid materials, Plenum Press, New York, pp 690–691
33. Zhao D, Feng J, Huo Q, Melosh N, Fredrickson GH, Chmelka BF, Stucky GD (1998) Science 279:548–552
34. Zhao D, Huo Q, Feng J, Chmelka BF, Stucky GD (1998) J Am Chem Soc 120:6024–6036
35. Wu S, Han Y, Zou YC, Song JW, Zhao L, Di Y, Liu SZ, Xiao FS (2004) Method. Chem Mater 16:486–492
36. Aburto J, Ayala M, Bustos-Jaimes I, Montiel C, Terres E, Dominguez JM, Torres E (2005) Microporous Mesoporous Mater 83:193–200
37. Cheng CF, Lin YC, Cheng HH, Chen YC (2003) Chem Phys Lett 382:496–501
38. Van Der Voort P, Benjelloun M, Vansant EF (2002) J Phys Chem B 106:9027–9032
39. Luan Z, Maes EM, Van der Heide PAW, Zhao D, Czernuszewicz RS, Kevan L (1999) Chem Mater 11:3680–3686
40. Klien S, Weckhuysen BM, Martens JA, Maier WF, Jacobs PA (1996) Homogeneity of titania–silica mixed oxides: detailed UV–DRS-studies as function of titania-content. J Catal 163:489-491
41. Petrini G, Cesana A, De Alberti GF, Genoni G, Leofanti M, Padovan M, Paparatto G, Roffia P (1991) Deactivation phenomena on ti-silicalite. Stud Surf Sci Catal 68:761-766
42. Balaji SY (2006) Raman Spectrosc 37:1416–1422
43. Bassi AL, Cattaneo D, Russo V, Bottani CE, Barborini E, Mazza T, Piseri P, Milani P, Ernst FO, Wegner K, Pratsinis SEJ (2005) Appl Phys 98:074305–074305-9
44. Reyes P, Aguirre MC, Pecchi G, Fierro JLG (2000) J Mol Catal A 164(1–2):245–251
45. Tian H, Zhang T, Sun X, Liang D, Li L (2001) Appl Catal A 210(1–2):55–62
46. Jia J, Zhou J, Zhang C, Yuan Z, Wang S, Cao L, Wang S (2008) Appl Catal A 341(1–2):1–7
47. Haneda M, Fujitani T, Hamada H (2006) J Mol Catal A 256(1–2):143–148
48. Amrousse R, Katsumi T, Niboshi Y, Azuma N, Bachar A, Hori K (2013) Appl Catal A 452:64-68
49. Yoshida A, Takahashi Y, Ikeda T, Azemoto K, Naito S (2011) Catal Today 164(1):332–335
50. Atuchin VV, Kesler VG, Pervukhina NV, Zhang Z (2006) J Electron Spectrosc Relat Phenom 152(12):18–24
51. LaVopa V, Satterfield CN (1988) J Catal 110:375–387
52. Furimsky E, Massoth FE (1999) Catal Today 52:381–495
53. Laredo G, De los Reyes J, Cano L, Castillo J (2001) Appl Catal A 207:103-112
54. Beltramone AR, Resasco DE, Alvarez WE, Choudhary TV (2008) Ind Eng Chem Res 47:19
55. Santikunaporn M, Herrera J, Jongpatiwut S, Resasco DE, Alvarez WE, Sughrue EL (2004) J Catal 228:100
56. Amezcua JC, Salcedo C, Puente I, Dominguez J, Klimova T (2005) Catal Today 107–108:578–588
57. Vít Z (2007) Appl Catal A 322:142–151
58. Harvey TG, Pratt KC (1989) Appl Catal 47:335–341
59. Dong D, Jeong S, Massoth FE (1997) Catal Today 37:267–275
60. Muegge B, Massoth FE, Bartholomew CH, Butt JB (Eds.) (1991) Catalyst Deactiv 68:297-304
61. Yang SH, Satterfield CN (1984) Ind Eng Chem Proc Des Dev 23:20–25
62. Dalla Betta RA, Boudart M (1973) Preparation and catalytic activity. In: Proceedings 5th international congress on catalysis, vol 2. North Holland, Amsterdam, pp 1329–1341
63. Yoshimura Y, Toba M, Matsui T, Harada M, Ichihashi Y, Bando KK, Yasuda H, Ishihara H, Morita Y, Kameoka T (2007) Appl Catal A 322:152–171
64. Klimova T, Rodríguez E, Martínez M, Ramírez J (2001) Microporous Mesoporous Mater 44–45:357–365
65. Foger KE, Anderson JR (1979) J Catal 59(3):325–339
66. Srivastava R, Srinivas D, Ratnasamy P (2006) Microporous Mesoporous Mater 90:314–326

67. Saikia L, Satyarthi JK, Srinivas D, Ratnasamy P (2007) J Catal 252:148–160
68. Srivastava R, Srinivas D, Ratnasamy P (2005) J Catal 233:1–15
69. Srinivas D, Srivastava R, Ratnasamy P (2004) Materials design in catalysis. Catal Today 96(3):127–133
70. Klimova T, Gutiérrez O, Lizama L, Amezcua J (2010) Microporous Mesoporous Mater 133:91–99
71. Arata K, Akutagawa S, Tanabe K (1976) Bull Chem Soc Jpn 49:390–393
72. Wang I, Chang WF, Shiau RJ, Wu JC, Chung CS (1983) J Catal 83:428–436
73. Lin TB, Jan CA, Chang JR (1995) Ind Eng Chem Res 34:4284–4289
74. Rousset JL, Stievano L, Cadete Santos Aires FJ, Geantet C, Renouprez AJ, Pellarin M (2001) J Catal 202:163–168